Chinese Journal of Structural Chemistry

ARTICLE

Contributions of Cs and Rb on Inhibiting Photo-induced Phase Segregation and Enhancement Optoelectronic Performances of $MA_{1-y}X_yPbI_{1.8}Br_{1.2}$ (X = Cs, Rb) Single Crystals

Qing Yao[1], Kaiyu Wang[1], Jie Zhang[1], Changqian Li[1], Chenyu Shang[1], Feitong Chen[1], Qi Huang[1], Qiqi Zhao[1], Weiwei Zhang[1], Xiaoyuan Zhan[1] and Jianxu Ding[1]*

[1]*College of Materials Science and Engineering, Shandong University of Science and Technology, Qingdao 266590, China*

ABSTRACT Introducing inorganic cation into hybrid organic-inorganic perovskites (HOIPs) has attracted great attention because of the enhancement stabilities without sacrificing their excellent optoelectronic properties. Here, we introduce Cs and Rb into $MAPbI_{1.8}Br_{1.2}$ single crystals (SCs) to dig out the mixed cation effect on optoelectronic performances and phase stabilities. Both Rb and Cs can increase the lattice capacity, which is sufficient to relieve the lattice stress caused by photon energy, thus achieving the purpose of stabilizing the lattice structure and inhibiting migration of halide ions, compared with $MAPbI_{1.8}Br_{1.2}$ SC. On the other hand, the smaller polarity of Rb and Cs reduces the electron-phonon coupling, thus significantly inhibiting the migration of halide ions. Meanwhile, through planar photo-detectors, $MA_{0.9}Cs_{0.1}PbI_{1.8}Br_{1.2}$-based device behaves much excellent optoelectronic performance (R = 0.170 A/W, EQE = 51.39 %, $D^* = 4.42 \times 10^{12}$ Jones, on/off ratio: ~522).

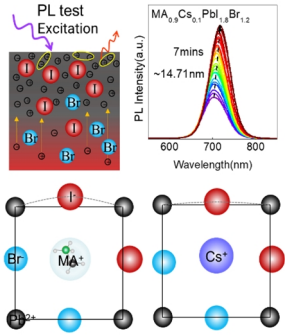

Keywords: perovskite single crystal, photo-induced phase segregation, mixed A-cation, optoelectronic performances

n INTRODUCTION

Due to the advantages of large absorption coefficient, small exciton binding energy, high carrier mobility, adjustable band gap and easy manufacturing, organic-inorganic hybrid metal halide perovskites $CH_3NH_3PbX_3$ (X = I, Br, Cl) have attracted much attention as light absorbers for optoelectronic devices.[1-5] Till now, the power conversion efficiency (PCE) of perovskite solar cells has reached a record of 25.5%.[6] However, the application and development of perovskite optoelectronic devices still face many difficulties, such as instability and toxicity of lead, etc.[7-9] Improving the stability and optoelectronic property of perovskites is greatly demanded for further commercial applications.[10-11]

To improve the stability and optoelectronic property of perovskites, many efforts have been made, among which mixed halide is one of the most effective methods.[12-14] For instance, mixed halide can regulate the absorption range and band gap of $MAPbBr_{3-x}Cl_x$ and $MAPbI_{3-x}Br_x$ perovskites covering the entire UV-visible region.[15] Besides, mixed halide can adjust carrier diffusion dynamics. It was reported that in $MAPbI_{3-x}Br_x$ perovskite films, the carrier diffusion rate of photo-generated carriers is dependent on Br content.[16] It should be noted that in the mixed halide perovskites, the molar ratio of halides should be strictly controlled. Unsuitable mixed halide ratio brings fatal defect of photo-induced phase segregation, which ultimately induces instability in the mixed halide perovskites. Draguta et al[17] quantitatively analyzed the phase segregation process of $MAPbI_{3-x}Br_x$ perovskites using spectral measurement and theoretical modeling. They believed that the phase segregation driving force is the I-rich phase with the reduction of band gap, and phase segregation could be suppressed by deliberately designing carrier diffusion length and injected carrier concentration. Byun reported the optical and structural properties of mixed halide perovskite $MAPbBr_{3-x}I_x$ SCs to investigate the underlying mechanisms of the light soaking effect and found that the photo-induced phase segregation is completely reversible.[18]

To suppress photo-induced phase segregation in the mixed halide perovskites, various strategies are proposed, among which partial replacement of organic cation (MA, FA) by smaller polarity of inorganic cations (Cs, Rb) can reduce the electron-phonon coupling and inhibit halide segregation.[19-21] Bischak[22] demonstrated that photo-induced phase segregation is an intrinsic property of mixed halide perovskites, and the segregation severity and dynamics depend on the electron-phonon coupling strength. Knight[23] provided evidence for low-barrier ionic pathways in $MAPb(Br_{0.5}I_{0.5})_3$, which brought rearrangement of halide ions in localized region. In contrast, $FA_{0.83}Cs_{0.17}Pb(Br_{0.4}I_{0.6})_3$ lacks such low-barrier ionic pathways and is, consequently, more stable against halide segregation. Compared with perovskite films, perovskite SCs have lower defect densities and no grain boundary, so it is expected that the photo-induced phase segregation effect might be different from that in film.[24-27] Nonetheless, the photo-induced phase segregation mechanism in perovskite SCs is still unclear yet.

Doping I in $MAPbBr_3$ perovskite can effectively control the crystal band gap, but a large amount of I doping will lead to the crystal structure from cubic phase ($MAPbBr_3$) to tetragonal phase ($MAPbI_3$). Thus, we controlled the I content to about 60%. To clarify the mechanism of phototropic phase segregation in perovskite SCs, here we successfully grow a series of $MA_{1-y}X_yPbI_{1.8}Br_{1.2}$ (X = Rb, Cs) SCs to investigate the light soaking effect on SC. In particular, the photo-induced phase segregation is systematically investigated through PL, UV-vis and XRD, which testifies that

DOI: 10.14102/j.cnki.0254-5861.2022-0089

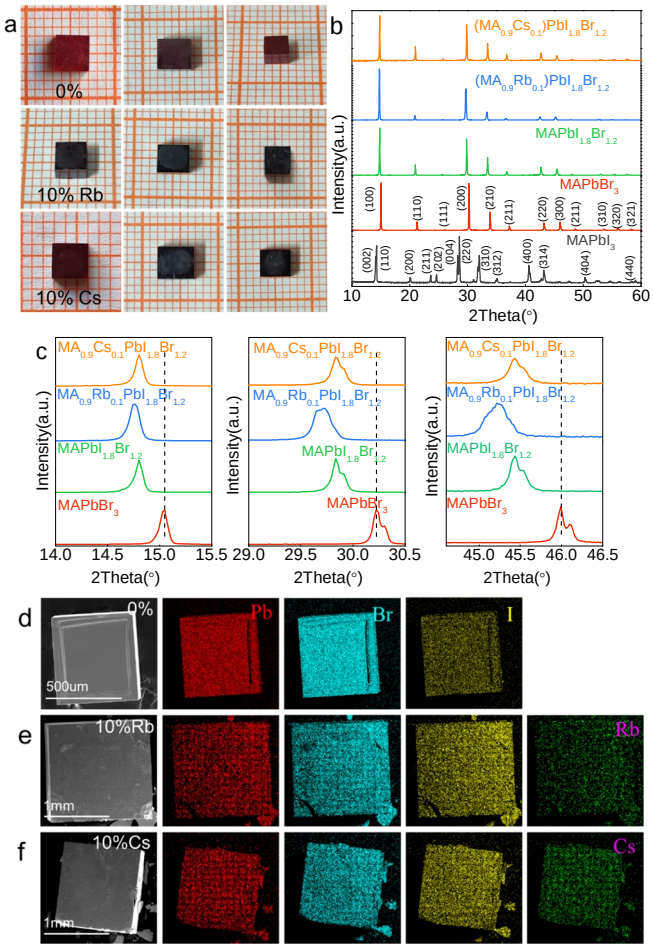

Figure 1. (a) Photographs of $MAPbI_{1.8}Br_{1.2}$, $MA_{0.9}Rb_{0.1}PbI_{1.8}Br_{1.2}$ and $MA_{0.9}Cs_{0.1}PbI_{1.8}Br_{1.2}$ SCs; (b-c) XRD patterns and enlarged XRD patterns of $MAPbI_3$, $MAPbBr_3$ and $MA_{1-y}X_yPbI_{1.8}Br_{1.2}$ powders; (d-f) Element distribution of $MAPbI_{1.8}Br_{1.2}$, $MA_{0.9}Rb_{0.1}PbI_{1.8}Br_{1.2}$ and $MA_{0.9}Cs_{0.1}PbI_{1.8}Br_{1.2}$ SCs, respectively.

phase segregation is a completely reversible process. In addition, Cs and Rb can significantly improve the optical stability, and effectively improve the crystal properties.

n RESULTS AND DISCUSSION

Figure 1a shows photographs of $MA_{1-y}X_yPbI_{1.8}Br_{1.2}$ SCs, whose shapes are similar cubic. The crystal color is related with the crystal thickness, which gradually transforms from black red to black because of the thickness related transmittance. For instance, the color of $MA_{0.9}Cs_{0.1}PbI_{1.8}Br_{1.2}$ SCs illustrated in Figure S1a testifies this phenomenon. Therefore, through controlling the growth time within 2-3 days, thinner $MA_{1-y}X_yPbI_{1.8}Br_{1.2}$ SCs are grown (Figure S1b-d), confirming that the thickness affects the color of crystals, which in turn affects the absorption of the crystals. Figure S2 shows the UV-vis absorption spectra of $MAPbI_{1.8}Br_{1.2}$ powder and the transmittance of $MAPbI_{1.8}Br_{1.2}$ SC at thicknesses of 1 and 2.5 mm. It is found that with the increase of crystal thickness, the transmittance decreased, and thus the absorption coefficient was enhanced.

In order to characterize the crystal structure, XRD patterns of $MAPbI_3$, $MAPbBr_3$ and $MA_{1-y}X_yPbI_{1.8}Br_{1.2}$ powders were carried out (Figure 1b). The diffraction peaks of $MA_{1-y}X_yPbI_{1.8}Br_{1.2}$ crystals correspond to cubic $MAPbBr_3$ and are different from that of tetrahedral $MAPbI_3$. According to the crystallization theory, lead halide and methylamine halide perovskite precursors can coordinate with organic solvent molecules to form complexes. Since Pb-I has weaker bond energy than Pb-Br, the coordination between PbI_2 and solvent is stronger than that of $PbBr_2$, resulting in $PbBr_2$-GBL complexes requiring higher temperatures to dissociate. Compared with PbI_2-GBL, the $PbBr_2$-GBL complexes are easier to dissociate at 60 °C, so that the content of Br in the precursor solution increases sharply and reaches the saturated state, and the grown single crystals are more inclined to the $MAPbBr_3$ structure. Therefore, the as-grown $MA_{1-y}X_yPbI_{1.8}Br_{1.2}$ crystals belong to cubic structure and $Pm\bar{3}m$ space group. Compared with $MAPbI_{1.8}Br_{1.2}$, incorporation of Rb or Cs increases the concentration of I into crystal lattice, causing the increase of I in the crystal. Thus, the color of $MA_{0.9}Cs_{0.1}PbI_{1.8}Br_{1.2}$ and $MA_{0.9}Rb_{0.1}PbI_{1.8}Br_{1.2}$ SCs are deeper than that of $MAPbI_{1.8}Br_{1.2}$, and the crystal lattices are expanded through the diffraction peak shift to the small angles (Figure 1c). By comparison with the X-site halide anion, the A-site mixed cations play a role of charge compensation in lattice and stabilize the crystal structure, contributing relatively little to the structural distortion.[28] Besides, we further investigate the stability of $MA_{1-y}X_yPbI_{1.8}Br_{1.2}$ perovskites at room temperature via XRD. As shown in Figure S3, after the $MA_{1-y}X_yPbI_{1.8}Br_{1.2}$ perovskites are placed in the air environment for 4 months, the diffraction peaks remain unchanged compared with the fresh samples, thereby confirming their good stability. Furthermore, the energy dispersive X-

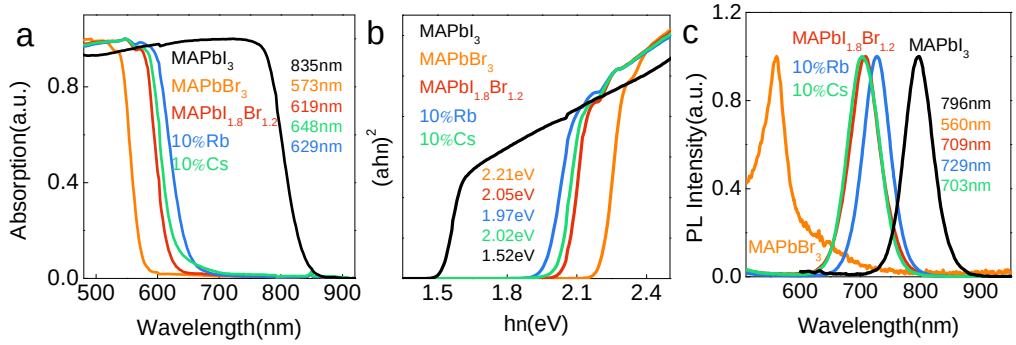

Figure 2. Optical performance of $MA_{1-y}X_yPbI_{1.8}Br_{1.2}$ crystals: (a) UV-vis absorption, (b) Optical band gaps, (c) Steady-state PL spectra.

DOI: 10.14102/j.cnki.0254-5861.2022-0089

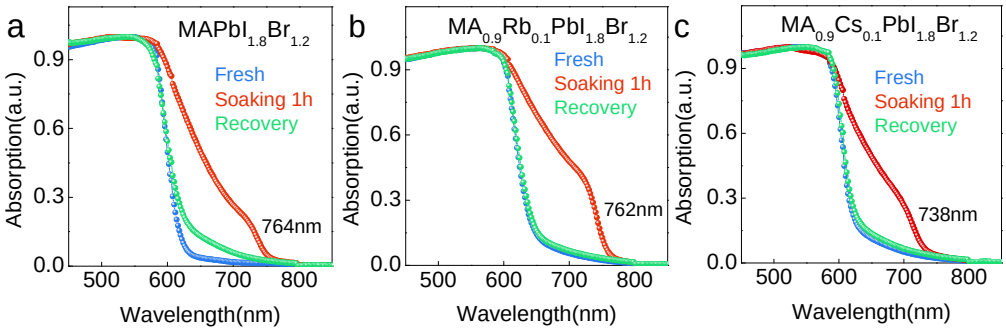

Figure 3. (a-c) UV-vis absorption of $MA_{1-y}X_yPbI_{1.8}Br_{1.2}$ before and after light illumination and after recovery.

ray spectrometer (EDS) in Figure 1(d-f) also shows that the I contents of the crystals with the addition of RbI or CsI are higher than that in $MAPbI_{1.8}Br_{1.2}$ SC, which is consistent with the XRD data.

Figure 2a shows the UV-vis absorption spectra of $MAPbI_3$, $MAPbBr_3$ and $MA_{1-y}X_yPbI_{1.8}Br_{1.2}$ crystal powders. Compared with $MAPbI_{1.8}Br_{1.2}$, redshift of the absorption onsets of $MA_{1-y}X_yPbI_{1.8}Br_{1.2}$ with incorporation of RbI or CsI occurs, and the corresponding optical band gaps are 2.05, 1.97 and 2.02 eV respectively, as shown in Figure 2b. The changes of band gaps and absorption onsets are attributed to the increase of I into crystal lattice. The main contribution of Cs and Rb cations adjusts the structural stability and electrical neutrality.[29] Therefore, the contribution of Rb and Cs to the optical absorption and band gap of the crystals is not as obvious as that of I, which is consistent with the results of XRD. It is worth noting that the PL emission peaks of $MA_{1-y}X_yPbI_{1.8}Br_{1.2}$ crystals are 709, 729 and 703 nm respectively, which have obvious Stokes shift compared with the absorption onsets (Figure 2c). In addition, under strong light illumination, the color of crystals changes from dark red to black (Figure S4), which means the phase segregation appears in the crystal under illumination, resulting in the emergence of I-rich region and thus bringing red shift of PL peaks.

Figure 3 shows absorption spectra of $MA_{1-y}X_yPbI_{1.8}Br_{1.2}$ crystals under strong light illumination (power density: 6 $mW{\cdot}cm^{-2}$) for 1 h. The absorption onsets of $MA_{1-y}X_yPbI_{1.8}Br_{1.2}$ crystals change significantly after 1 h illumination, and the absorption capacity of the crystals towards longer wavelength (730-760 nm) is significantly enhanced. However, the Rb and Cs can reduce the change of the absorption onsets of the crystals under illumination. The smaller polarity of Rb and Cs leads to weak interaction between free charge and ion lattice and form less polar lattice,[29] which can effectively inhibit ion migration (photo-induced phase segregation) under light illumination. Figure S4 shows the evolution process of $MA_{1-y}X_yPbI_{1.8}Br_{1.2}$ powders under continuous illumination, in which the color of $MA_{1-y}X_yPbI_{1.8}Br_{1.2}$ powders changes from black red to black. After the withdrawal of illumination for 3 hours, the absorption onsets recover to their original position and the color of the powders returns to its original color under environment conditions. This phenomenon indicates that photo-induced phase segregation is an almost reversible process,[30] and provides a promising prospect for the crystal in future commercial applications.

To better investigate the photo-induced phase segregation in $MA_{1-y}X_yPbI_{1.8}Br_{1.2}$ crystals, the in situ PL and XRD were carried out. As we all know, the halide ions in the crystal migrate when obtaining sufficient energy, and form I-rich and Br-rich regions.[31] Meanwhile, the activated carriers (electrons and holes) migrate to the I-rich region and recombine here, resulting in the redshift of PL positions (Figure 4). Obviously, from the PL spectra the PL peak of $MAPbI_{1.8}Br_{1.2}$ is ~18.73 nm redshifted after illumination, and the intensity is remarkably enhanced. However, the $MA_{1-y}X_yPbI_{1.8}Br_{1.2}$ crystals with Rb or Cs have significant lower redshift of ~15.89 and ~14.71 nm, respectively, as shown in Figure 4(b-d). Cs significantly reduces the trap density, as well as the secondary recombination rate of free mobile carriers in perovskite bulk materials. Furthermore, the trap states in Cs-containing perovskites are at shallow states. In contrast, the addition of Rb has only a minor impact on the trap states.[32] Therefore, the inhibition effect of Rb on photo-induced phase segregation is weaker than introducing Cs. In addition, the PL spectra of $MA_{1-y}X_yPbI_{1.8}Br_{1.2}$ SCs after illumination for 7 min and recovery for 30 min were investigated, as shown in Figure 5(a-c). It is found that the PL intensity of $MA_{1-y}X_yPbI_{1.8}Br_{1.2}$ SCs is significantly reduced after recovery for 30 min, confirming that the photo-induced phase segregation is an almost reversible process. After recovery, compared with $MAPbI_{1.8}Br_{1.2}$, the red shift of PL peaks of Rb and Cs doped crystals is not obvious, indicating that Rb and Cs inhibit the migration

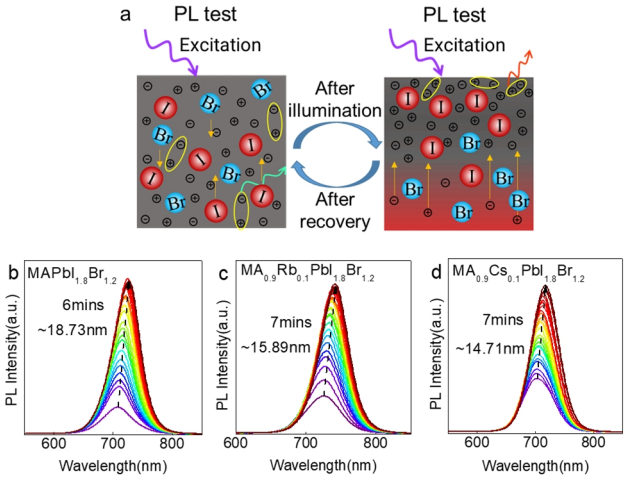

Figure 4. (a) Schematic of relevant kinetic processes during halide phase segregation; (b-d) PL spectra of $MA_{1-y}X_yPbI_{1.8}Br_{1.2}$, recorded under a wavelength of 445 nm.

DOI: 10.14102/j.cnki.0254-5861.2022-0089

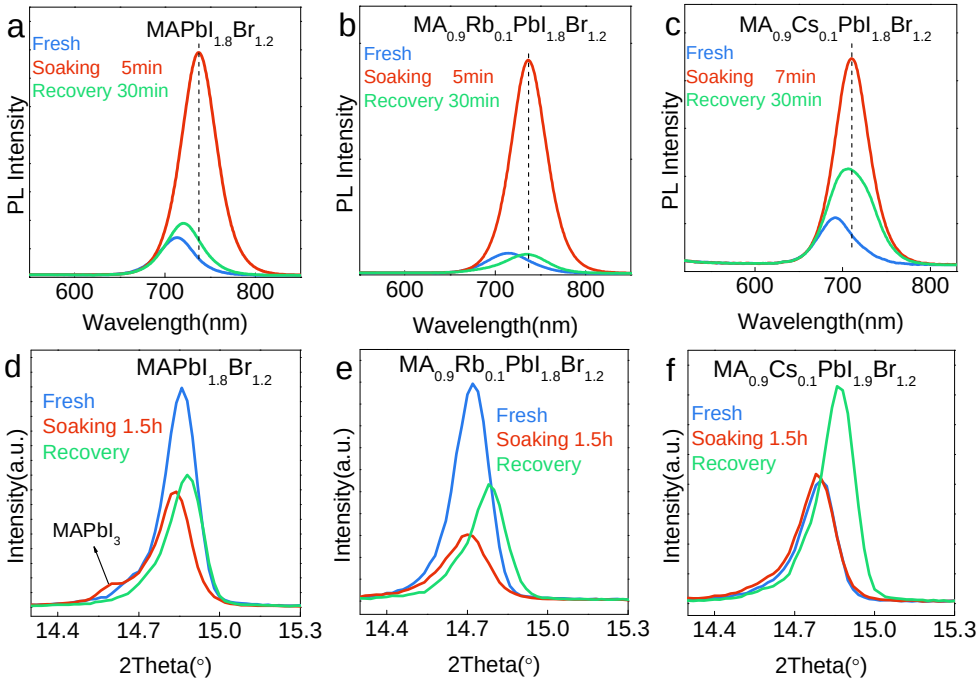

Figure 5. (a-c) PL spectra of fresh, soaking, and recovered $MA_{1-y}X_yPbI_{1.8}Br_{1.2}$, recorded under a wavelength of 445 nm; (d-f) XRD patterns of $MA_{1-y}X_yPbI_{1.8}Br_{1.2}$ before and after illumination intensity of 6 mW·cm^{-2} and a wavelength of 365 nm.

of halide ions not only in the light illumination but also during the recovery process.

On the other hand, through the XRD data in Figure S5, the diffraction peaks of $MAPbI_{1.8}Br_{1.2}$ and $MA_{0.9}Rb_{0.1}PbI_{1.8}Br_{1.2}$ decrease significantly after 1.5 h illumination due to the fact that illumination destroys the structures of the crystals to reduce the crystallinity. However, diffraction peaks of $MA_{0.9}Cs_{0.1}PbI_{1.8}Br_{1.2}$ crystals maintain stable after illumination, indicating that Cs is beneficial to stabilize the crystal structure, and the enhanced bonding between Cs and the inorganic metal skeleton.

The enlarged XRD of $MA_{1-y}X_yPbI_{1.8}Br_{1.2}$ is shown in Figure 5(d-f). For $MAPbI_{1.8}Br_{1.2}$, the diffraction peaks are obviously broadened and asymmetric under illumination, and an obvious diffraction peak at 14.6° belonging to $MAPbI_3$ crystal occurs, implying that $MAPbI_{1.8}Br_{1.2}$ crystals show phase segregation and form I-rich and Br-rich regions, and thus $MAPbI_3$ phase appears in the crystals. From the absorption spectra, it is noteworthy that the photo-induced phase segregation in $MAPbI_{1.8}Br_{1.2}$ crystals is reversible. Illumination stimulant ions migrate inside the crystals to from I- and Br-rich regions (Figure 6a), which increases the lattice stress (Figure 6c-d).[19] When illumination disappears, ions reversely migrate under the stress inside the crystal lattice and concentration gradient, and the redistribution of ions leads to a change in the lattice parameters. Non-uniform strains and local distortions associated with the halide distribution are in existence, which is manifested through the shift of diffraction peaks between fresh and recovered XRD. The recovery diffraction peaks shift towards larger angles implies that the recovered crystal lattice shrinks and shortens the inter-ion spacing. On the other hand, ion redistribution repairs shallow-level defects and improves crystal quality. After recovery, the diffraction peaks of 14.6° of $MAPbI_{1.8}Br_{1.2}$ crystal disappears, implying the redistribution of halide ions and disappearance of I-rich and Br-rich regions.

Nevertheless, no diffraction peaks of $MAPbI_3$ are detected in $MA_{0.9}Cs_{0.1}PbI_{1.8}Br_{1.2}$ and $MA_{0.9}Cs_{0.1}PbI_{1.8}Br_{1.2}$ in Figure 5(d-f), indicating that Rb and Cs improve the structural stability, which in turn improves the photo-stability. The smaller size of Rb and Cs compared with MA increases the lattice tolerance, which is sufficient to relieve the lattice stress, thus achieving the purpose of stabilizing the lattice structure and inhibiting the migration of halide ions, as shown in Figure 6b. On the other hand, the smaller polarity of Rb and Cs can reduce the electron-phonon coupling and

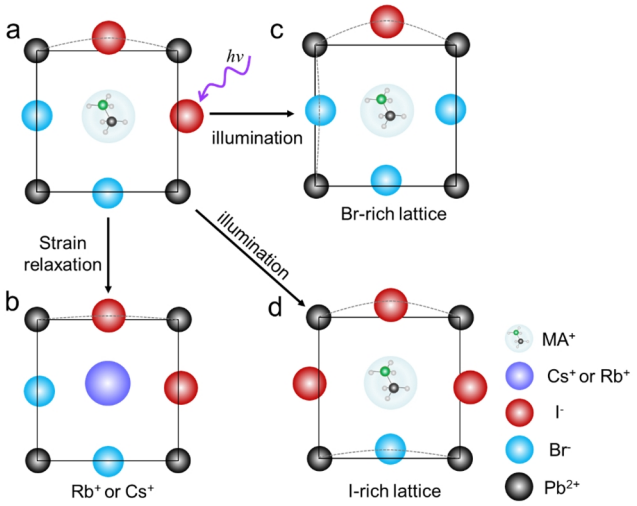

Figure 6. Schematic diagram of Rb and Cs inhibit phase segregation: (a) $MAPbI_{1.8}Br_{1.2}$ lattice; (b) $MA_{1-y}X_yPbI_{1.8}Br_{1.2}$ lattice; (c-d) Formation of Br- or I-rich regions in $MAPbI_{1.8}Br_{1.2}$ crystals.

DOI: 10.14102/j.cnki.0254-5861.2022-0089

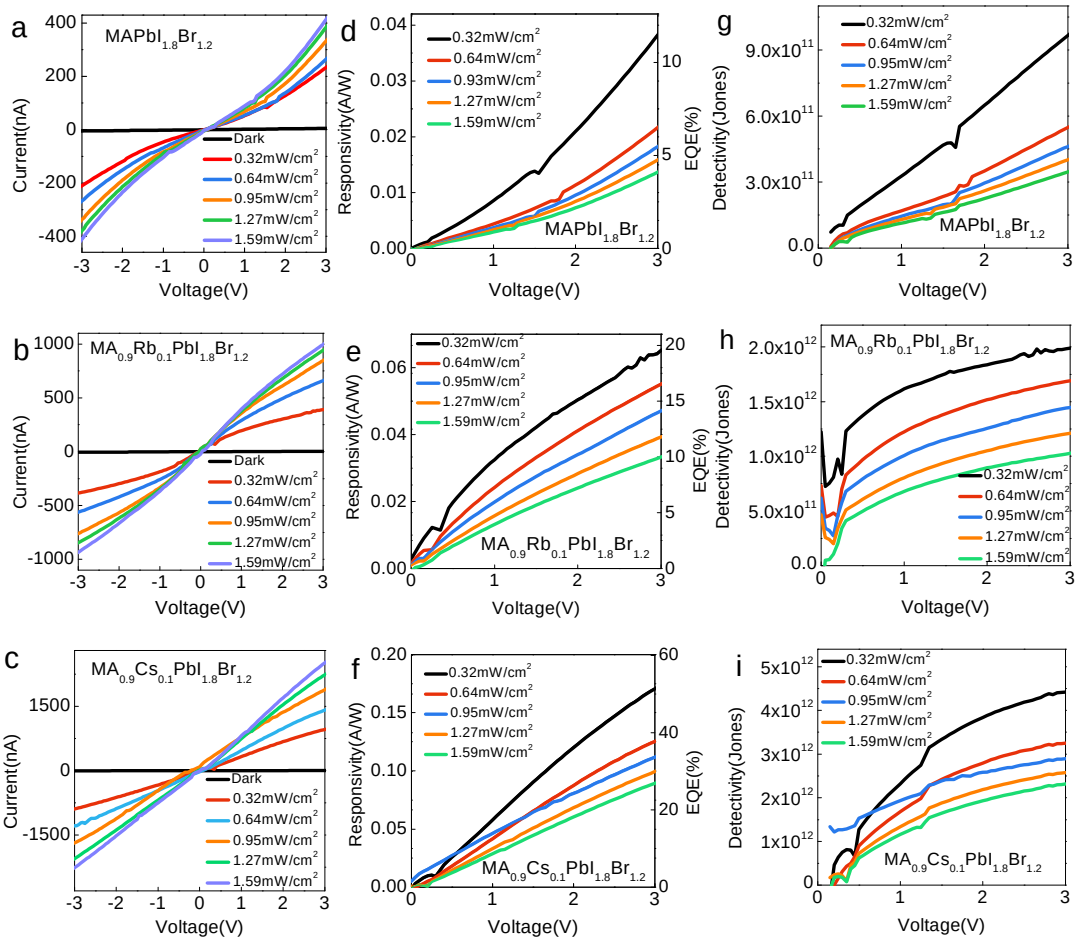

Figure 7. Optoelectronic properties of photo-detectors based $MA_{1-y}X_yPbI_{1.8}Br_{1.2}$ SCs: (a-c) Photocurrent; (d-f) Responsivities and EQEs; (g-i) Detectivities.

adjust the lattice distortion,[33-34] therefore significantly suppressing the migration of halide ions.

Besides, the diffraction peak intensity of $MA_{1-y}X_yPbI_{1.8}Br_{1.2}$ crystals after recovery increased significantly compared with those after illumination. The redistribution of ions after light withdrawal and Cs doping lead to the reduction of defects and carrier migration in the crystal lattice.[35] Therefore, the crystals recover to the stable phase and the crystallinity increases after the light withdrawal.

To dig out the roles of Cs and Rb on optoelectronic properties, planar photo-detectors were fabricated. Figure 7(a-c) depicts the I-V characteristics of the devices in the dark and under light illumination of 405 nm with various power densities. As an increase of power density, the photocurrent of the devices gradually increases. The dark current of $MA_{1-y}X_yPbI_{1.8}Br_{1.2}$ with Rb or Cs are 3.96 and 4.64 nA respectively at 3 V bias, lower than that of the $MAPbI_{1.8}Br_{1.2}$ SC (4.88 nA). In addition, the photocurrent of $MA_{1-y}X_yPbI_{1.8}Br_{1.2}$ SCs with Rb or Cs (996.60 nA, 2512.05 nA) is much larger than 413.15 nA for $MAPbI_{1.8}Br_{1.2}$. The enhancement of optoelectronic properties by Rb and Cs is ascribed to that Rb and Cs passivate the surface and eliminate surface defects, thereby hindering the recombination of carriers.[28] On the other hand, compared with MA, Rb and Cs have higher migration activation energies because of their stronger binding force with inorganic metal skeleton and result in better optoelectronic performances.

In addition, the responsivity (R), external quantum efficiency (EQE) and detectivity (D*) are the key parameters of the photo-detector and calculated according to the following equations:[36-37]

$$R = \frac{I_{ph}-I_{dark}}{P_{in}*S} \quad (1)$$

$$EQE = \frac{R*h*c}{e\lambda} \quad (2)$$

$$D^* = \frac{R}{\sqrt{2e*I_{dark}}} \quad (3)$$

Where I_{ph} and I_{dark} represent the photocurrent and dark current, P_{in} is the incident light intensity, S is the effective area of photo-detector, h is the Planck's constant, c is the speed of light, e is the elementary charge, and λ is the wavelength of the laser. The relationships of R, EQE and D* of $MA_{1-y}X_yPbI_{1.8}Br_{1.2}$ SCs with various illumination powers and bias are shown in Figure 7(d-i). The responsivity of $MAPbI_{1.8}Br_{1.2}$ photo-detector is about 0.038 A/W, while it is enhanced to 0.065 and 0.170 A/W of $MA_{0.9}Rb_{0.1}PbI_{1.8}Br_{1.2}$ and $MA_{0.9}Cs_{0.1}PbI_{1.8}Br_{1.2}$ SCs, respectively. The EQE values increased from 11.54% for the $MAPbI_{1.8}Br_{1.2}$ SC photo-detector to 19.65% and 51.39% for the $MA_{0.9}Rb_{0.1}PbI_{1.8}Br_{1.2}$ and $MA_{0.9}Cs_{0.1}PbI_{1.8}Br_{1.2}$ SCs photo-detectors. The D* of the photo-detector also

DOI: 10.14102/j.cnki.0254-5861.2022-0089

Table 1. Key Parameters of Others Halide Perovskite Photo-detectors

Devices	Light (nm)	Responsivity ($A \cdot W^{-1}$)	EQE (%)	D (Jones)	On-off ratio	Refs.
$MA_{0.9}Cs_{0.1}PbI_{1.8}Br_{1.2}$ SC	405	0.170	51.39	4.42×10^{12}	522	This work
$MAPb(I_{1-x}Br_x)_3$ films	532-808	0.331	50.3	4.27×10^{10}		[41]
$CH_3NH_3PbI_3$ film	405	12		6.5×10^{11}		[42]
$(FAPbI_3)_{1-x}(MAPbBr_3)_x$ films	254	0.15	25	7.21×10^{10}	337.14	[43]
$MAPbCl_3$ SC	365	0.047		1.2×10^{10}	1.1×10^3	[44]
$MA_{0.6}FA_{0.4}PbI_3$ film	775	0.27		1.49×10^{12}		[45]
$MAPbI_3$/UCns film		0.27	46	0.76×10^{12}	10^3	[46]
$MAPbI_3$ SC	405	0.019	6.55	1.0×10^{11}	17	[47]
$MAPbBr_3$ SC	405	0.038	0.113		55	[48]

increased from 9.66×10^{11} Jones in $MAPbI_{1.8}Br_{1.2}$ SC to 1.99×10^{12} and 4.42×10^{12} Jones in $MA_{0.9}Rb_{0.1}PbI_{1.8}Br_{1.2}$ and $MA_{0.9}Cs_{0.1}PbI_{1.8}Br_{1.2}$ SCs under 405 nm. Rb and Cs significantly improve the responsivity and detectivity of the crystal, because Rb and Cs improve the photo-stability and passivate the surface to reduce defects and improve the crystal quality.[38-40] As a result, the optoelectronic properties of the crystal are enhanced. Table 1 lists the intrinsic optoelectronic properties of other organic-inorganic halide perovskite photo-detectors, implying $MA_{1-y}X_yPbI_{1.8}Br_{1.2}$ SCs have excellent optoelectronic properties.

Transient photo-response is one of the key parameters of optoelectronic devices. To illustrate the transient photo-response of $MA_{1-y}X_yPbI_{1.8}Br_{1.2}$ SCs photo-detectors, we measured the current-time (I-t) curves of the photo-detectors. As shown in Figure 8(a-c), switching cycles illustrate a reproducible photocurrent response with good cycling stability. For $MAPbI_{1.8}Br_{1.2}$ SC device, the highest on-off ratio is 89 under 1.5 V bias, which is enhanced to 201 ($MA_{0.9}Rb_{0.1}PbI_{1.8}Br_{1.2}$) and 522 ($MA_{0.9}Cs_{0.1}PbI_{1.8}Br_{1.2}$), respectively. The enhancement of on-off ratios is considered to be ascribed to the higher photocurrent. In $MAPbI_{1.8}Br_{1.2}$, halide ions migrate to form more defects in the crystal under illumination and electric field, causing poor optoelectronic performance. While Rb and Cs inhibit ion migration, and improve the light tolerance of $MA_{1-y}X_yPbI_{1.8}Br_{1.2}$ SCs, optical stability, and the optoelectronic performance of the device.

n CONCLUSION

In summary, the contributions of Cs and Rb in $MA_{1-y}X_yPbI_{1.8}Br_{1.2}$ SCs on photo-induced phase segregation and optoelectronic performance are investigated. The introduction of Rb and Cs into the crystal lattice effectively alleviates the photo-induced phase segregation, inhibits defect formation and improves the optoelectronic performance of devices.

n EXPERIMENTAL

Chemicals. Methylamine (CH_3NH_2, 40 wt%) was purchased from Kelon Chemical Reagent Factory. Hydroiodic acid (HI, 47 wt%), lead iodide (PbI_2, 98%), and cesium iodide (CsI,99.9%) were obtained from Macklin. Hydrobromic acid (HBr, 40 wt%), rubidium iodide (RbI, 99.9%), N,N-dimethylformamide (DMF, 99.8%) and γ-butyrolactone (GBL, 99%) and lead bromide ($PbBr_2$, 99%) were commercially available from Aladdin. MAI and MABr were synthesized according to the previous report.[49-50]

Growth of $MAPbI_3$, $MAPbBr_3$ and $MA_{1-y}X_yPbI_{1.8}Br_{1.2}$ SCs. The equal mole ratio MAI (or MABr) and PbI_2 (or $PbBr_2$) were dissolved in 5 mL GBL (or DMF) solvent, and 1 M yellow transparent solution (or the transparent colorless solution) was obtained by continuous stirring at room temperature. After 3-4 days, centimeter-grade $MAPbI_3$ (or $MAPbBr_3$) SCs were obtained at 100 and 60 °C, as shown in Figure S6(a-b). $MA_{1-y}X_yPbI_{1.8}Br_{1.2}$ SCs can be obtained by dissolving MABr and PbI_2 in a solvent mixture of GBL and DMF (volume ratio GBL:DMF = 5:1) in the designed ratio to obtain 0.8 M clear solution. Then, 10% RbI and CsI were added to the solution, the yellow transparent solution was sealed and heated to 60 °C. Large-scale $MA_{1-y}X_yPbI_{1.8}Br_{1.2}$ SCs can be obtained within 2-5 days as shown in Figure S7(a-c).

Devices Fabrications. The planar photo-detectors with interdigitated Au electrodes (150 μm interdigital width) were fabricated on the polished (100) crystal facet of $MA_{1-y}X_yPbI_{1.8}Br_{1.2}$ SCs by thermal evaporation (VZZ-300, Vnano), using an interdigitated mask (3×3 mm^2) placed on the (100) facet.

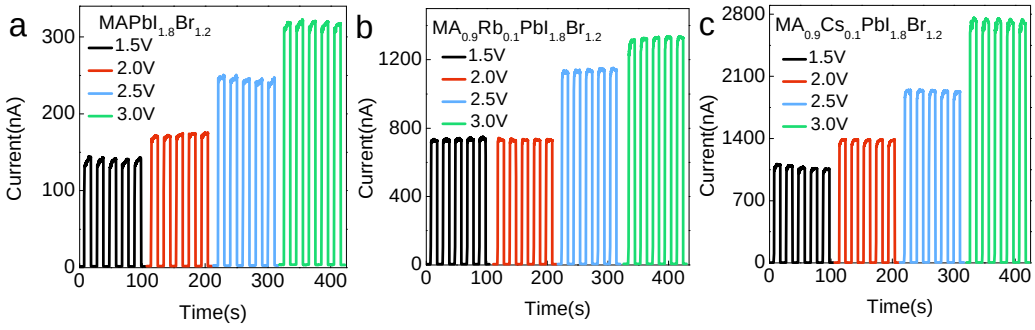

Figure 8. (a-c) Continuous on-off circles under different applied voltages of the photo-detector devices on (100) planes.

DOI: 10.14102/j.cnki.0254-5861.2022-0089

Characterizations. The XRD patterns of $MA_{1-y}X_yPbI_{1.8}Br_{1.2}$ crystal powders were collected on X-ray diffractometer (D/Max 2500 PC, CuKα radiation with wavelength of 0.154 nm). UV-vis absorption spectra of $MA_{1-y}X_yPbI_{1.8}Br_{1.2}$ crystal powders were recorded by UV-8000 spectrophotometer. The in-situ photoluminescence (PL) spectrum was recorded by Ocean Optics QE65000 spectrometer. A series of photocurrents of the planar photo-detectors based on $MA_{1-y}X_yPbI_{1.8}Br_{1.2}$ SCs were obtained by the electrical characteristic measurement system (Keithley 2450) under illumination using 405 nm InGaN-based semiconductor diodes. Besides this, the continuous on/off photocurrents under various applied voltages were harvested through setting the on/off interval time (20 s). All measurements were conducted in a dark space in order to eliminate the effect of light on the experiments.

n ACKNOWLEDGEMENTS

This work was financially supported by the National Natural Science Foundation of China (No. 52072225). The author gratitude the environmental and function material team, supported by the Project of Shandong Province Higher Educational Young Innovative Talent Introduction and Cultivation.

n AUTHOR INFORMATION

Corresponding author. Email: dingjianxu@sdust.edu.cn

n COMPETING INTERESTS

The authors declare no competing financial interest.

n ADDITIONAL INFORMATION

The descriptions of photographs of $MA_{1-y}X_yPbI_{1.8}Br_{1.2}$ SCs, UV-absorption spectra and transmittance of different thicknesses of $MAPbI_{1.8}Br_{1.2}$ SCs, stability of $MA_{1-y}X_yPbI_{1.8}Br_{1.2}$ at room temperature, photographs of $MA_{1-y}X_yPbI_{1.8}Br_{1.2}$ powders with light and recovery at different times, XRD patterns of $MA_{1-y}X_yPbI_{1.8}Br_{1.2}$ samples before illumination, after blue-violet light illumination and after recovery, growth of $MAPbI_3$ and $MAPbBr_3$ SCs, and growth process and photographs of thinner $MA_{1-y}X_yPbI_{1.8}Br_{1.2}$ SCs.

n ADDITIONAL INFORMATION

Supplementary information is available for this paper at http://manu30.magtech.com.cn/jghx/EN/10.14102/j.cnki.0254-5861.2022-0089

For submission: https://mc03.manuscriptcentral.com/cjsc

n REFERENCES

(1) Liu, N.; Huang, C. Y.; Zhu, L.; Chen, Y.; Xu, G. W.; Chu, L.; Ma, X. G. Organic cation effect on the physical properties of $CH_3NH_3PbI_3$ perovskite from the first-principles study. *Chin. J. Struct. Chem.* **2016**, 35, 1297-1305.

(2) Tao, J. L.; Wang, Z. W.; Wang, H. W.; Shen, J. L.; Liu, X. N.; Xue, J. W.; Guo, H. S.; Fu, G. S.; Kong, W. G.; Yang, S. P. Additive engineering for efficient and stable $MAPbI_3$-perovskite solar cells with an efficiency of over 21%. *ACS Appl. Mater. Interfaces* **2021,** 13, 44451-44459.

(3) Wang, Y.; Zhu, L. P.; Du, C. F. Polarization-sensitive light sensors based on a bulk perovskite $MAPbBr_3$ single crystal. *Materials* **2021**, 14, 1238.

(4) Jiang, S.; Wu, C. C.; Li, F.; Zhang, Y. Q.; Zhang, Z. H.; Zhang, Q. H.; Chen, Z. J.; Qu, B.; Xiao, L. X.; Jiang, M. L. Machine learning (ML)-assisted optimization doping of KI in $MAPbI_3$ solar cells. *Rare Met.* **2020**, 40, 1-10.

(5) Mao, G. P.; Wang, W.; Shao, S.; Sun, X. J.; Chen, S. A.; Li, M. H.; Li, H. M. Research progress in electron transport layer in perovskite solar cells. *Rare Met.* **2018**, 2, 95-106.

(6) Min, H.; Lee, D. Y.; Kim, J.; Kim, G.; Lee, K. S.; Kim, J.; Paik, M. J.; Kim, Y. K.; Kim, K. S.; Kim, M. G.; Shin, T. J.; Seok, S. I. Perovskite solar cells with atomically coherent interlayers on SnO_2 electrodes. *Nature* **2021**, 598, 444-450.

(7) Wang, R.; Wang, J. T.; Tan, S.; Duan, Y.; Wang, Z. K.; Yang, Y. Opportunities and challenges of lead-free perovskite optoelectronic devices. *Trends Chem.* **2019**, 1, 368-379.

(8) Lee, J. W.; Dai, Z. H.; Han, T. H.; Choi, C.; Chang, S. Y.; Lee, S. J.; Marco, N. D.; Zhao, H. X.; Sun, P. Y.; Huang, Y.; Yang, Y. 2D perovskite stabilized phase-pure formamidinium perovskite solar cells. *Nat. Commun.* **2018**, 9, 3021.

(9) Gu, H.; Chen, C. S.; Zheng, Q. D. Long-term stable 2D Dion-Jacobson phase perovskite photodiode with low dark current and high on/off ratio. *Chin. J. Struct. Chem.* **2021**, 40, 1621-1630.

(10) Liu, Y.; Han, S. G.; Wang, J. Q.; Ma, Y.; Guo, W. Q.; Huang, X. Y.; Luo, J. H.; Hong, M. C.; Sun, Z. H. Spacer cation alloying of a homoconformational carboxylate trans isomer to boost in-plane ferroelectricity in a 2D hybrid perovskite. *J. Am. Chem. Soc.* **2021**, 143, 2130-2137.

(11) Li, M. F.; Han, S. G.; Liu, Y.; Luo, J. H.; Hong, M. C.; Sun, Z. H. Soft perovskite-type antiferroelectric with giant electrocaloric strength near room temperature. *J. Am. Chem. Soc.* **2020**, 142, 20744-20751.

(12) Li, Y. B.; Yang, T.; Xu, Z. Y.; Liu, X. T.; Huang, X. Y.; Han, S. G.; Liu, Y.; Li, M. F.; Luo, J. H.; Sun, Z. H. Dimensional reduction of $Cs_2AgBiBr_6$: a 2D hybrid double perovskite with strong polarization sensitivity. *Angew. Chem. Int. Ed.* **2020**, 59, 3429-3433.

(13) Wang, Y. T.; Guan, X. W.; Chen, W. J.; Yang, J.; Hu, L.; Yang, J.; Li, S.; Zadeh, K. K.; Wen, X. M.; Wu, T. Illumination-induced phase segregation and suppressed solubility limit in Br-rich mixed-halide inorganic perovskites. *ASC Appl. Mater. Interfaces* **2020**, 12, 38376-38385.

(14) Chen, Y. Y.; Gao, C. H.; Yang, T.; Li, W. J.; Xu, H. J.; Sun, Z. H. Research advances of ferroelectric semiconductors of 2D hybrid perovskites toward photoelectronic applications. *Chin. J. Struct. Chem.* **2022**, 41, 2204001-2204011.

(15) Fang, Y.; Dong, Q.; Shao, Y.; Yuan, Y.; Huang, J. Highly narrowband perovskite single-crystal photodetectors enabled by surface-charge recombination. *Nat. Photonics* **2015**, 9, 679–686.

(16) Shi, W. J.; Wang, Y.; Zhang, T. Y.; Zhang, H. J.; Zhao, Y. X.; Chen, J. Fast charge diffusion in $MAPb(I_{1-x}Br_x)_3$ films for high-efficiency solar cells revealed by ultrafast time-resolved reflectivity. *J. Phys. Chem. A* **2019**, 123, 2674-2678.

(17) Draguta, S.; Sharia, O.; Yoon, S. J.; Brennan, M. C.; Morozov, Y. V.; Manser, J. S.; Kamat, P. V.; Schneider, W. F.; Kuno, M. Rationalizing the light-induced phase segregation of mixed halide organic-inorganic perovskites. *Nat. Commun.* **2017**, 8, 1-8.

(18) Byun, H. R.; Park, D. Y.; Oh, H. M.; Namkoong, G.; Jeong, M. S. Light soaking phenomena in organic-inorganic mixed halide perovskite single crystals. *ACS Photonics* **2017**, 4, 2813-2820.

(19) Sutter-Fella, C. M.; Ngo, Q. P.; Cefarin, N.; Gardner, K. L.; Tamura, N.; Stan, C. V.; Drisdell, W. S.; Javey, A.; Toma, F. M.; Sharp, I. D. Cation-dependent light-induced halide demixing in hybrid organic-inorganic perovskites. *Nano Lett.* **2018**, 18, 3473-3480.

(20) Zhang, S.; Tang, M. C.; Fan, Y. Y.; Li, R. P.; Nguyen, N. V.; Zhao, K.; Anthopoulos, T. D.; Hacker, C. A. Role of alkali-metal cations in electronic structure and halide segregation of hybrid perovskites. *ACS Appl. Mater. Interfaces* **2020**, 12, 34402-34412.

(21) Wang, K. Y.; Yao, Q.; Zhang, J.; Shang, C. Y.; Li, C. Q.; Chen, F. T.;

Zhou, T. L.; Sun, H. Q.; Zhang, W. W.; Zhu, H. L.; Ding, J. X. Short-range migration of A-site cations inhibit photoinduced phase segregation in $FA_xMA_yCs_{1-x-y}PbI_{3-z}Br_z$ single crystals. *J. Phys. Chem. C* **2021**, 125, 23050-23057.
(22) Bischak, C. G.; Wong, A. B.; Lin, E.; Limmer, D. T.; Yang, P. D.; Ginsberg, N. S. Tunable polaron distortions control the extent of halide demixing in lead halide perovskites. *J. Phys. Chem. Lett.* **2018**, 9, 3998-4005.
(23) Knight, A. J.; Borchert, J.; Oliver, R. D. J.; Patel, J. B.; Radaelli, P. G.; Snaith, H. J.; Johnston, M. B.; Herz, L. M. Halide segregation in mixed-halide perovskites: influence of A-site cations. *ACS Energy Lett.* **2021**, 6, 799-808.
(24) Doherty, T. A. S.; Winchester, A. J.; Macpherson, S.; Johnstone, D. N.; Pareek, V.; Tennyson, E. M.; Kosar, S.; Kosasih, F. U.; Anaya, M, Abdi-Jalebi, M.; Andaji-Garmaroudi, Z.; Wong, E. L.; Madeo, J.; Chiang, Y. H.; Park, J. S.; Jung, Y. K.; Petoukhoff, C. E.; Divitini, G.; Man, M. K. L.; Ducati, C.; Walsh, A.; Midgley, P. A.; Dani, K. M.; Stranks, S. D. Performance-limiting nanoscale trap clusters at grain junctions in halide perovskites. *Nature* **2020**, 580, 360-366.
(25) Jiang, J.; Sun, X.; Chen, X. C.; Wang, B. W.; Chen, Z. Z.; Hu, Y.; Guo, Y. W.; Zhang, L. F.; Ma, Y.; Gao, L.; Zheng, F. S.; Jin, L.; Chen, M.; Ma, Z. W.; Zhou, Y. Y.; Padture, N. P.; Beach, K.; Terrones, H.; Shi, Y. F.; Gall, D.; Lu, T. M.; Wertz, E.; Feng, J.; Shi, J. Carrier lifetime enhancement in halide perovskite via remote epitaxy. *Nat. Commun.* **2019**, 10, 4145.
(26) Chen, J.; Morrow, D. J.; Fu, Y. P.; Zheng, W. H.; Zhao, Y. Z.; Dang, L. N.; Stolt, M. J.; Kohler, D. D.; Wang, X. X.; Czech, K. J.; Hautzinger, M. P.; Shen, S. H.; Guo, L. J.; Pan, A.; Wright, J. C.; Jin, S. Single-crystal thin films of cesium lead bromide perovskite epitaxially grown on metal oxide perovskite ($SrTiO_3$). *J Am. Chemical Soc.* **2017**, 139, 13525-13532.
(27) Makarov, S.; Furasova, A.; Tiguntseva, E.; Hemmetter, A.; Berestennikov, A.; Pushkarev, A.; Zakhidov, A.; Kivshar, Y. Halide-perovskite resonant nanophotonics. *Adv. Opt. Mater.* **2019**, 7, 1800784.
(28) Xue, J. J.; Wang, R.; Chen, X.; Yao, C. L.; Jin, X. Y.; Wang, K. L.; Huang, W. C.; Huang, T. Y.; Zhao, Y. P.; Zhai, Y. X.; Meng, D.; Tan, S.; Liu, R. Z.; Wang, Z. K.; Zhu, C. H.; Zhu, K.; Beard, M. C.; Yan, Y. F.; Yang, Y. Reconfiguring the band-edge states of photovoltaic perovskites by conjugated organic cations. *Science* **2021**, 371, 636-640.
(29) Frost, J. M. Calculating polaron mobility in halide perovskites. *Phys. Rev. B: Condens. Matter Mater. Phys.* **2017**, 96, 195202.
(30) Tang, X. F.; Berg, M. V. D.; Gu, E.; Horneber, A.; Matt, G. J.; Osvet, A.; Meixner, A. J.; Zhang, D.; Brabec, C. J. Local observation of phase segregation in mixed-halide perovskite. *Nano Lett.* **2018**, 18, 2172-2178.
(31) Li, Z.; Zheng, X.; Xiao, X.; An, Y. K.; Wang, Y. B.; Huang, Q. Y.; Li, X.; Cheacharoen, R. R.; An, Q. Y.; Rong, Y. G.; Wang, T.; Xu, H. X. Beyond the phase segregation: probing the irreversible phase reconstruction of mixed-halide perovskites. *Adv. Sci.* **2021**, 2103948.
(32) Hu, Y. H.; Hutter, E. M.; Rieder, P.; Grill, I.; Hanisch, J.; Aygüler, M. F.; Hufnagel, A. G.; Handloser, M.; Bein, T.; Hartschuh, A.; Tvingstedt, K.; Dyakonov, V.; Baumann, A.; Savenije, T. J.; Petrus, M. L.; Docampo, P. Understanding the role of cesium and rubidium additives in perovskite solar cells: trap states, charge transport, and recombination. *Adv. Energy Mater.* **2018**, 8, 1703057.
(33) Mattoni, A.; Filippetti, A.; Caddeo, C. Modeling hybrid perovskites by molecular dynamics. *J. Phys.: Condens. Matter* **2017**, 29, 043001.
(34) Zheng, K.; Zhu, Q.; Abdellah, M.; Messing, M. E.; Zhang, W.; Generalov, A.; Niu, Y.; Ribaud, L.; Canton, S. E.; Pullerits, T. Exciton binding energy and the nature of emissive states in organometal halide perovskites. *J. Phys. Chem. Lett.* **2015**, 6, 2969-2975.
(35) Damle, V. H.; Gouda, L.; Tirosh, S.; Tischler, Y. R. Structural characterization and room temperature low-frequency Raman scattering from $MAPbI_3$ halide perovskite films rigidized by cesium incorporation. *ACS Appl. Energy Mater.* **2018**, 1, 6707-6713.
(36) Cheng, X. H.; Yuan, Y.; Jing, L.; Zhou, T. L.; Li, Z. X.; Peng, Z. W.; Yao, Q.; Zhang, J.; Ding, J. X. Nucleation-controlled growth of superior long oriented $CsPbBr_3$ microrod single crystals for high detectivity photodetectors. *J. Mater. Chem. C* **2019**, 7, 14188.
(37) Wang, Y. C.; Zhang, Y. M.; Liu, Y. T.; Pang, T. Q.; Hu, Z. Y.; Zhu, Y. J.; Luan, S. Z.; Jia, R. X. Temperature-dependence studies of organolead halide perovskite-based metal/semiconductor/metal photodetectors. *RSC Adv.* **2017**, 7, 20206-20211.
(38) Park, I. J.; Seo, S.; Park, M. A.; Lee, S.; Kim, D. H.; Zhu, K.; Shin, H.; Kim, J. Y. Effect of rubidium incorporation on the structural, electrical, and photovoltaic properties of methylammonium lead iodide-based perovskite solar cells. *ACS Appl. Mater. Interfaces* **2017**, 9, 41898-41905.
(39) Du, S. J.; Jing, L.; Cheng, X. H.; Yuan, Y.; Ding, J. X.; Zhou, T. L.; Zhan, X. Y.; Cui, H. Z. Incorporation of cesium ions into $MA_{1-x}Cs_xPbI_3$ single crystals: crystal growth, enhancement of stability, and optoelectronic properties. *J. Phys. Chem. Lett.* **2018**, 9, 5833-5839.
(40) Ding, J. X.; Du, S. J.; Zhou, T. L.; Yuan, Y.; Cheng, X. H.; Jing, L.; Yao, Q.; Zhang, J.; He, Q. K.; Cui, H. Z.; Zhan, X. Y.; Sun, H. Q. Cesium decreases defect density and enhances optoelectronic properties of mixed $MA_{1-x}Cs_xPbBr_3$ single crystal. *J. Phys. Chem. C* **2019**, 123, 14969-14975.
(41) Qiao, S.; Liu, Y.; Liu, J. H.; Fu, G. S.; Wang, S. F. High-responsivity, fast, and self-powered narrowband perovskite heterojunction photodetectors with a tunable response range in the visible and near-infrared region. *ACS Appl. Mater. Interfaces* **2021**, 13, 34625-34636.
(42) Subramanian, A.; Akram, J.; Hussain, S.; Chen, J.; Qasim, K.; Lei, W. High-performance photodetector based on a graphene quantum dot/$CH_3NH_3PbI_3$ perovskite hybrid. *ACS Appl. Electron. Mater.* **2020**, 2, 230-237.
(43) Nguyen, T. M. H.; Lee, S. K.; Kim, S.; Bark, C. W. Practical demonstration of deep-ultraviolet detection with wearable and self-powered halide perovskite-based photodetector. *ACS Appl. Mater. Interfaces* **2021**, 13, 57609-57618.
(44) Maculan, G.; Sheikh, A. D.; Abdelhady, A. L.; Saidaminov, M. I.; Haque, M. A.; Murali, B.; Alarousu, E.; Mohammed, O. F.; Wu, T.; Bakr, O. M. $CH_3NH_3PbCl_3$ single crystals: inverse temperature crystallization and visible-blind UV-photodetector. *J. Phys. Chem. Lett.* **2015**, 6, 3781-3786.
(45) Maity, A.; Raychaudhuri, A. K.; Ghosh, B. Paper-based stable broad optical detector made from cation organic perovskite halides. *J. Phys. Chem. C* **2021**, 125, 10646-10652.
(46) Li, J. B.; Shen, Y. L.; Liu, Y. C.; Shi, F.; Ren, X. D.; Niu, T. Q.; Zhao, K.; Liu, S. Z. Stable high-performance flexible photodetector based on up-conversion nanoparticles/perovskite microarrays composite. *ACS Appl. Mater. Interfaces* **2017**, 9, 19176-19183.
(47) Ding, J. X.; Jing, L.; Cheng, X. H.; Zhao, Y.; Du, S. J.; Zhan, X. Y.; Cui, H. Z. Design growth of $MAPbI_3$ single crystal with (220) facets exposed and its superior optoelectronic properties. *J. Phys. Chem. Lett.* **2018**, 9, 216-221.
(48) Zuo, Z. Y.; Ding, J. X.; Zhao, Y.; Du, S. J.; Li, Y. F.; Zhan, X. Y.; Cui, H. Z. Enhanced optoelectronic performance on the (110) lattice plane of an $MAPbBr_3$ single crystal. *J. Phys. Chem. Lett.* **2017**, 8, 684-689.
(49) Ding, J. X.; Du, S. J.; Cheng, X. H.; Jing, L.; Zhao, Y.; Zuo, Z. Y.; Cui, H. Z.; Zhan, X. Y. Anisotropic optoelectronic performances on (112) and (100) lattice plane of perovskite $MAPbI_3$ single crystal. *Mater. Chem. Phys.* **2018**, 204, 222-227.
(50) Wang, K. Y.; Yao, Q.; Zhang, J.; Jing, L.; Cheng, X. H.; Shang, C. Y.; Li, C. Q.; Chen, F. T.; Zhou, T. L.; Zhu, H. L.; Li, T. X.; Li, H. P.; Wang, Z. W.; Ding, J. X. How ternary cations and binary halogens stabilize trigonal $FA_{1-x-y}MA_xCs_yPbI_{3-z}Br_z$ perovskites: from a single crystal perspective. *Chem. Mater.* **2022**, 34, 1179-1190.

Received: April 18, 2022
Accepted: May 7, 2022
Published: May 20, 2022

DOI: 10.14102/j.cnki.0254-5861.2022-0089